Journal of Marine Science and Engineering

Article

The Effect of the Layout of a Rigid Splitter Plate on the Flow-Induced Vibration of a Downstream Cylinder Subjected to Wake Flow

Li Ruan, Dingyong Yu *, Jian Bao and Jinxin Zhao

College of Engineering, Ocean University of China, Qingdao 266100, China; rl19980729@163.com (L.R.); baojian0319@163.com (J.B.); jxzhao_ouc@163.com (J.Z.)
* Correspondence: dyyu01@ouc.edu.cn

Abstract: In this study, the effect of additional positions of rigid splitter plates on the response characteristics of tandem cylinders at a Reynolds number of 150 and a fixed distance ratio of 5.0 was numerically investigated via the computational fluid dynamics (CFD) method. Four layouts for the cylinder–plate body, including a downstream cylinder (DC), a downstream cylinder–plate body with a wake side plate (DCP), a downstream plate–cylinder body with an incoming flow side plate (DPC), and a downstream plate–cylinder–plate body with a double-sided plate (DPCP), are considered. The results show that the splitter plate attached to the incoming flow side or the wake side can suppress the vibration of the downstream cylinder in a specific reduced velocity range ($4.0 < U_r \leq 10.0$). Compared with the DC, the maximum response amplitude of the DPC and DCP in the lock-in region is reduced by 30.8% and 47.4%, and the lock-in bandwidth is also significantly narrower. The layer separation point of the upstream cylinder moves downstream upon adding splitter plates to both the incoming flow and wake sides, and the resulting splitter shear layer of the DPCP is completely parallel to the free flow, while the maximum response amplitude is reduced by 93.6%, which realizes the best effect of stream-induced vibration suppression.

Keywords: flow induced vibration; wake interference; splitter plate; computational fluid dynamic

Citation: Ruan, L.; Yu, D.; Bao, J.; Zhao, J. The Effect of the Layout of a Rigid Splitter Plate on the Flow-Induced Vibration of a Downstream Cylinder Subjected to Wake Flow. *J. Mar. Sci. Eng.* **2023**, *11*, 2138. https://doi.org/10.3390/jmse11112138

Academic Editor: José António Correia

Received: 19 October 2023
Revised: 2 November 2023
Accepted: 7 November 2023
Published: 9 November 2023

1. Introduction

With the development of offshore oil exploration from shallow sea to deep sea, offshore platforms are also developing from fixed tower platforms in shallow water areas to large deep-water floating platforms, of which the riser system is one of the key structures. When the ocean current flows through the riser, the periodic vortex shedding on both sides of the riser will induce its vibration response. This interaction between the current and riser is called vortex-induced vibration (VIV), which is a typical flow-induced vibration (FIV) phenomenon. The resulting repeated vibration processes will induce fatigue problems and reduce the service life of the riser and even cause the fracture of the riser [1,2].

The advantage of VIV is that it can be used as a renewable energy [3], but the disadvantage of it is that it adversely affects the safety of offshore structures. Early research mainly focused on VIV suppression. Both passive control and active control are the suppression methods used [4]. Active control requires a large amount of external energy input, high costs, and complex technology [5]. Comparatively, passive control can change the wake structure and even eliminate vortex shedding through the installation of simple auxiliary devices, thus weakening the vortex-induced force [6–10]. As a passive control device for the flow control of blunt body structures, rigid splitter plates have been widely studied [4]. Earlier, Roshko [11] carried out an experimental study on the flow around a fixed cylinder impact due to the length of a rigid splitter plate under a Reynolds number of 20,000 and discovered that it could effectively reduce the drag force through the attachment of a splitter plate to the wake side of the cylinder. And in a certain plate length range, it can also completely inhibit the vortex shedding of the cylinder. Other scholars' research results have also demonstrated the correctness of this conclusion [12,13]. Following on from this, the application of rigid splitter plates has attracted considerable attention in the field of VIV suppression. Hu et al. [14] conducted wind tunnel experiments on a flexibly mounted cylinder–plate body, in which the Re = 4000~48,000 and the relative plate length L/D in the range of 0.4~2.0 was considered. They found that when $L/D \leq 1.0$, the VIV of the cylinder could not be suppressed by the splitter plate, and only if the splitter plate was long enough ($L/D \geq 1.5$) could it yield an excellent suppression effect. Sun et al. [15] studied the vibration characteristics of the cylinder with an additional rigid splitter plate through numerical simulation in a laminar flow (Re = 100). With an increase in plate length, three response modes of VIV, VIV coupling gallop, and VIV separated with galloping were distinguished successively. Meanwhile, three different vortex-shedding modes of 2S, P + S, and 2P were captured. Zhu and Liu [16] numerically studied the effect of a wavy rigid splitter plate on a cylinder at a low Reynolds number (Re = 150), and they found that the wave-shaped splitter plates could effectively inhibit the initiation and lower branches of VIV, reducing the average drag coefficient and the root mean square lift coefficient by 27.5% and 54.9%, respectively. Moreover, in some cases, the presence of a splitter plate can lead to galloping instability in the structure. Galloping is another crucial phenomenon in FIV besides VIV, which consists of the feature in which the reduced velocity and the response amplitude are inversely related and the vibration frequency is constant and low [17–20]. Zhu et al. [21] studied the effect of a splitter plate on the FIV of a cylinder at a low Reynolds number (Re = 120) by using a numerical method. According to the simulation results, when the reduced velocity $U_r \leq 9.0$, the VIV of the cylinder could be inhibited by the splitter plate, and when $U_r > 9.0$, the reattachment of the shear layer on the splitter plate would generate additional lift force. This may result in a galloping response induced by the cylinder. Cui et al. [22] investigated the influence of rigid and flexible splitter plates on cylindrical FIV by conducting flume experiments (Re = 1680~8720). They observed that with the addition of a rigid shunt plate, the cylinder produced two response modes of VIV and galloping, and the amplitude increased with the increase in U_r. Diaz-Ojeda et al. [23] used numerical simulation to study the effect of immersion depth on a stationary cylinder with a flexible splitter plate. In addition, the parametric space composed of Reynolds (Re = 100~1000), Cauchy ($Cy = 1.11 \times 10^{-3}$~5.26×10^{-5}), and Froude numbers (Fr = 2~3.5) was also set as the key factor. Their research shows that the response of the flexible splitter plate increases with the increase in the immersion depth, and the amplitude of the end of the flexible splitter plate increases with the increase in Re, Cy, and Fr. Sahu et al. [24] numerically studied the effect of mass ratio m^* ($2 \leq m^* \leq 1000$) on a cylinder–plate body at a Reynolds number of 150. They observed that the U_r at the start of the galloping response increased with the increase in m^*.

In addition, some scholars have also changed the additional position of the splitter plate to study the impact of the incoming flow side splitter plate on the VIV of the cylinder. Sun et al. [25] conducted a collection of flume experiments (Re = 1100~7700) to explore the influence of an incoming flow side splitter plate (L/D = 0~3.6) on an elastically mounted cylinder. They found that when water flows through the cylinder–plate body, a time-varying high-pressure region is formed near the tip of the splitter plate on the incoming flow side. This high-pressure region generates an added damping force which is always opposite to the movement of the cylinder, thereby suppressing the vibration of the cylinder. The longer the splitter plate, the better the suppression effect. Dehkordi and Jafari [6] numerically studied the hydrodynamic characteristics of a cylinder when the detached splitter plate is situated at the wake side of the cylinder under a low Reynolds number (Re = 100 or 150). They observed that the further away the splitter plate was from the cylinder, the greater the pressure on the backflow side of the cylinder, but the drag force and Strouhal number of the cylinder were gradually reduced. Zhu et al. [21] used numerical simulation to investigate the impact of the splitter plate position on the FIV of a single cylinder under a low Reynolds number (Re = 120) and discovered that placing the splitter plate upstream of the cylinder could delay the beginning of vortex shedding, narrow the wake bandwidth, and ultimately suppress the vibration of the cylinder. Amini and Zahed [26] studied the influence of rigid splitter plates on the FIV of tandem double-cylinder systems through numerical simulation at Re = 150, m^* = 2. Three configurations were considered, including attaching splitters only to the upstream cylinder, attaching splitters only to the downstream cylinder, and attaching splitters to two cylinders at the same time. The results show that in most cases, the system will have a galloping response. Assia et al. [27] investigated the effect of a splitter plate device that rotates around a cylinder on VIV in a flume experiment. The results show that the splitter plate not only reduces the drag of the cylinder, but also plays a great role in suppressing VIV. In the range of the experimental Reynolds number (up to 30,000), the drag of the additional rotating splitter plate cylinder is about 60% of the drag of the bare cylinder.

The above-mentioned publications have proven that splitter plates demonstrate good performance in terms of suppressing the FIV of a single cylinder, but studies addressing concerns about the galloping problems induced by the different attachment modes of the splitter plate are still limited. Meanwhile, multi-cylinder systems are extensively used in practical engineering applications, but most of the current research about vibration suppression via splitter plates focuses on single-cylinder systems. To address these issues, this paper conducts a numerical study of the influence of the splitter plate layout on the FIV of tandem cylinder systems. The remainder of this paper is organized as follows: Section 2 provides the research object, numerical method, and the related evaluation parameters. Section 3 verifies the feasibility of the numerical model. In Section 4, the numerical results of cylinder–plate bodies with different splitter plate layouts are discussed in detail. The final summary of the significant conclusions of this study is presented in Section 5.

2. Numerical Model

2.1. Cylinder–Plate Model

In this study, the fixed upstream cylinder and the elastically mounted downstream cylinder have the identical diameter, D. The downstream cylinder–plate body is modelled as a single-degree-of-freedom mass–spring–damper system, which is merely permitted to vibrate freely in the cross-flow direction as water flows by. As shown in Figure 1, the diagrams of different layouts including the downstream cylinder (DC), the downstream cylinder–plate body with a wake side plate (DCP), the downstream plate–cylinder body with an incoming flow side plate (DPC), and the downstream plate–cylinder–plate body with a double-sided plate (DPCP) are listed, where D represents the diameter of the cylinder, L_d represents the length of the wake-side splitter plate, and L_u represents the length of the incoming-flow-side splitter plate. G represents the distance between the centers of the cylinders. To achieve an optimal suppression effect, relatively long plate lengths were selected: the incoming flow side plate length L_u/D = 1.5 and the wake side plate length L_d/D = 1.5. Additionally, the spacing ratio (G/D = 5.0) remains fixed and the mass of the splitter plate is considered.

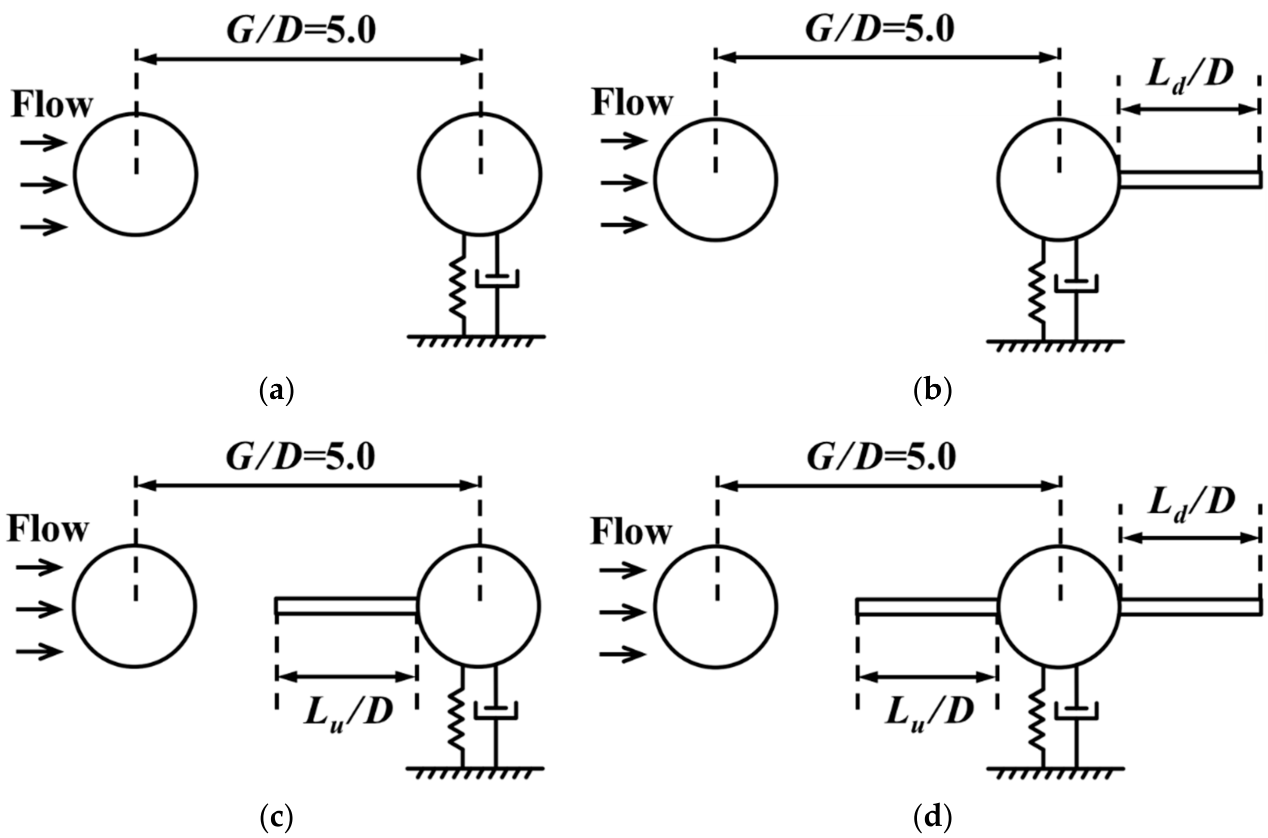

Figure 1. Diagram of the cylinder–plate body in different additional positions. (**a**) DC; (**b**) DCP; (**c**) DPC; (**d**) DPCP.

2.2. Hydrodynamic Parameters and Governing Equations

The reduced velocity U_r is expressed as:

$$U_r = \frac{U}{f_n D} \tag{1}$$

where f_n is the natural frequency of the downstream circular cylinder and U_r is the free-flow speed; this paper changes the reduced velocity by altering the spring stiffness [28], and the value range of the reduced velocity is U_r = 1.0~40.0.

This study introduces the dimensionless amplitude $A*$, frequency ratio $f*$, drag coefficient C_D, and lift coefficient C_L of the downstream cylinder–plate body, which are expressed as:

$$A* = \frac{(y_{\max} - y_{\min})}{2D} \tag{2}$$

$$f* = \frac{f_y}{f_n} \tag{3}$$

$$C_D = \frac{F_x}{\frac{1}{2}\rho U^2 DL} \tag{4}$$

$$C_L = \frac{F_y}{\frac{1}{2}\rho U^2 DL} \tag{5}$$

where $y_{\max}$ and $y_{\min}$ are the maximum and minimum transverse displacement of the downstream circular cylinder, respectively. In addition, f_y is the vibration frequency of the downstream circular cylinder. F_x and F_y are the drag force and lift force, respectively.

The fluid governing equations for unsteady and incompressible two-dimensional laminar flows are expressed as:

$$\frac{\partial u_i}{\partial x_i} = 0 \tag{6}$$

$$\frac{\partial u_i}{\partial t} + u_j \frac{\partial u_i}{\partial x_j} = -\frac{1}{\rho}\frac{\partial p}{\partial x_i} + v\frac{\partial^2 u_i}{\partial x_j \partial x_j} \tag{7}$$

where x_i represents the coordinates in the direction i, u_i represents the velocity in the direction x_i, t represents the flow time, p represents the pressure, ρ represents the fluid density, and ν is the kinematic viscosity.

The elastic installation of a two-dimensional cylinder–plate body can be simplified as a mass–spring–damping system, which only considers the movement of the cross-flow direction. The dimensionless equation of cylinder–plate body motion can be described as:

$$\ddot{Y} + \frac{4\pi\zeta}{U_r}\dot{Y} + \frac{4\pi^2}{U_r^2}Y = \frac{C_L}{\kappa m*} \tag{8}$$

where Y, $\dot{Y}$, and $\ddot{Y}$ represent the dimensionless displacement, dimensionless velocity, and dimensionless acceleration of the cylinder–plate body in the cross-flow direction, respectively, κ is the non-dimensional area coefficient for the cylinder–plate model, $\kappa = \frac{\pi}{2} + \frac{2hL}{D^2}$, and $m*$ is the mass ratio.

The rigid cylinder–plate body is regarded as a particle which moves on the x-y plane; then, Equation (6) can be expressed as:

$$\begin{cases} \frac{dY(t)}{dt} = V(t) \\ \frac{dV(t)}{dt} = \frac{C_l(t)}{\kappa m*} - \frac{4\pi\zeta}{U_r}V(t) - \frac{4\pi^2}{U_r^2}Y(t) \end{cases} \tag{9}$$

Equation (9) is described by the fourth-order Runge–Kutta method and expressed as follows:

$$\begin{cases} Y(t_{n+1}) = Y(t_n) + \Delta t \cdot V(t) + \frac{\Delta t^2}{6}(K_1 + K_2 + K_3) \\ V(t_{n+1}) = V(t) + \frac{\Delta t}{6}(K_1 + K_2 + K_3 + K_4) \end{cases} \tag{10}$$

in which

$$\begin{cases} K_1 = \frac{C_l(t)}{\kappa m*} - \frac{4\pi\zeta}{U_r}V(t) - \frac{4\pi^2}{(U_r^2)}Y(t) \\ K_2 = \frac{C_l(t)}{\kappa m*} - \frac{4\pi\zeta}{U_r}\left[V(t) + \frac{\Delta t}{2}K_1\right] - \frac{4\pi^2}{(U_r^2)}\left[Y(t) + \frac{\Delta t}{2}V(t)\right] \\ K_3 = \frac{C_l(t)}{\kappa m*} - \frac{4\pi\zeta}{U_r}\left[V(t) + \frac{\Delta t}{2}K_2\right] - \frac{4\pi^2}{(U_r^2)}\left[Y(t) + \frac{\Delta t}{2}V(t) + \frac{(\Delta t)^2}{4}K_1\right] \\ K_4 = \frac{C_l(t)}{\kappa m*} - \frac{4\pi\zeta}{U_r}[V(t) + \Delta t \cdot K_3] - \frac{4\pi^2}{(U_r^2)}\left[Y(t) + \Delta t \cdot V(t) + \frac{(\Delta t)^2}{2}K_2\right] \end{cases} \tag{11}$$

where K_1, K_2, K_3, and K_4 are the fourth-order Runge–Kutta transition functions and Δt and n are the time step and the number of time steps, respectively.

2.3. Numerical Mesh and Boundary Conditions

For the numerical simulation carried out in this paper, the computational fluid dynamics (CFD) software ANSYS-Fluent 2022 R1 was adopted, and the finite volume method and pressure separation solver were used to solve the Navier–Stokes (N-S) equation of incompressible flow. The pressure–velocity coupling equation was solved by the SIMPLEC algorithm [29]. The residual convergence criteria was set to 10^{-5}. The non-dimensional time step was set to 0.005 during the simulation and the Reynolds number Re = 150.

The computational domain is a rectangle with dimensions of 47D and 24D along the in-line and cross-flow directions, as shown in Figure 2. The distance between the two lateral boundaries and the fixed upstream cylinder is 12D, and the two lateral boundaries are set as the slip wall boundaries. The distance between the pressure outlet boundary and the fixed upstream cylinder is 35*D* to ensure full development of the vortex formation and shedding. The velocity inlet boundary condition is set to 12*D* from the left side of the fixed upstream cylinder. The overset mesh method is used to handle the dynamic mesh, which allows the component mesh to move relatively or partially overlap on the background mesh [30,31]. The data transfer between the component grid and the background grid is realized by interpolation calculation [32], so as to realize the movement of the cylinder–plate body in the calculation domain. The computational domain grid is a structured grid, and the background grid and the component grid are generated independently. The background grid is the entire rectangular computational domain, which remains static throughout the computation. The component grid includes the fixed upstream cylinder grid and the downstream cylinder–plate body grid. During the entire calculation process, the upstream circular cylinder grid stays static while the cylinder–plate body grid moves with the structure, and the data are transferred to the background mesh by interpolation. In order to accurately capture boundary-layer separation and vortex shedding, the grid near the fixed upstream cylinder, the downstream cylinder–plate body, and the wake region are encrypted. The encryption area is set wide enough to ensure that the component mesh has enough interpolation points with the background mesh during the entire motion process to achieve the effective transmission of flow field information between the two domains.

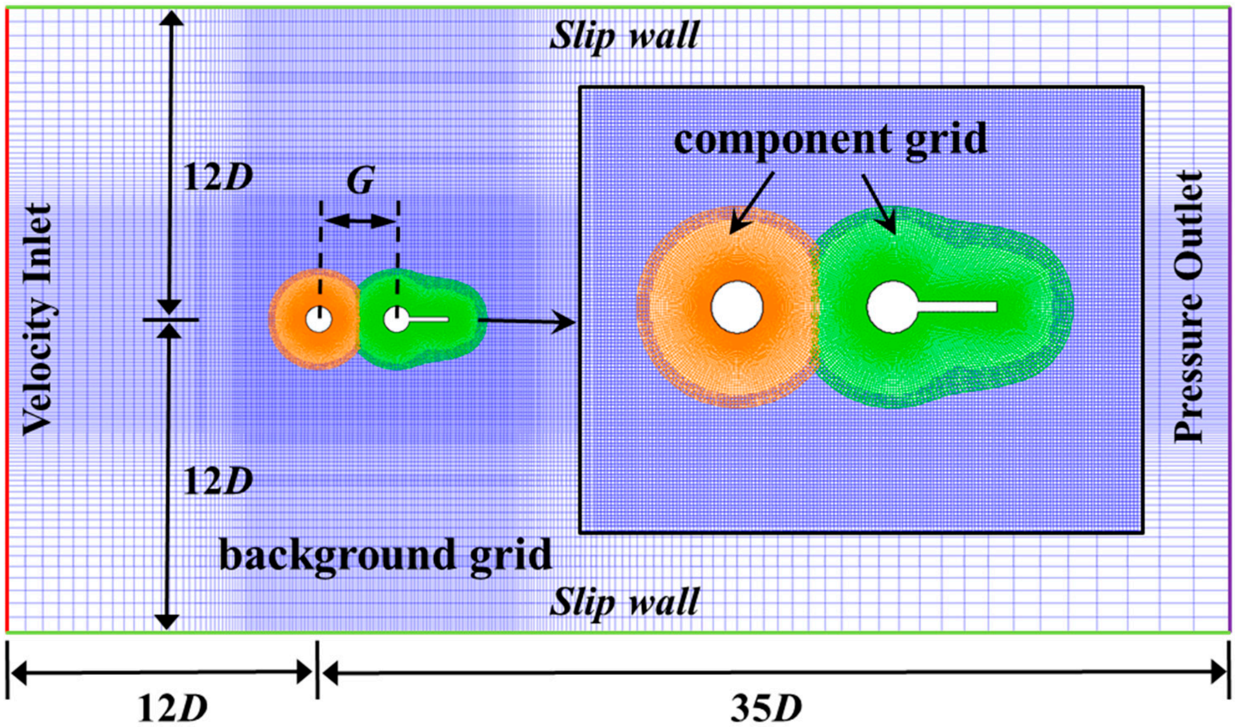

Figure 2. Grid and boundary condition settings diagram of the computing domain.

In the calculation process, the flow field of the background domain is updated by solving the N-S equation, and the data of background domain are transmitted to the component domain through the interpolation method. Then, the pressure of the structure in the component domain is solved by the same method. At the same time, the resultant force on the surface of the structure is obtained through integration, and the resultant force is substituted into the motion equation to obtain the structure displacement. The flow field in the component domain is restored, and then, the data are transmitted back to the background grid through the interpolation method. The above calculation process is repeated to simulate the FIV of the cylinder.

3. Numerical Model Validation

3.1. Grid Independence Verification

The mesh density of the numerical model has an impact on the computational time and computational accuracy. Therefore, four different mesh quantities (M1, M2, M3, and M4) were tested for grid independence [24], and three important parameters, including circumferential nodes N_c, component mesh elements N_{pe}, and background mesh elements N_{be}, were considered [30]. The computational results are shown in Table 1. By comparing the differences between A^*, f^*, $C_{D\text{-}ave}$, $C_{L\text{-}rms}$, and computation cost per cycle, it can be seen that the A^*, $C_{D\text{-}ave}$ and $C_{L\text{-}rms}$ of M1 and M4 are significantly different, and the maximum difference is 3.53% ($C_{L\text{-}rms}$). As the number of grids increases, the difference between M2 and M4 in various indexes decreased, the maximum difference was 1.03% ($C_{L\text{-}rms}$), and the maximum difference between M3 and M4 was 0.73% ($C_{L\text{-}rms}$), indicating that the impact of further increasing the number of grids on the calculation results was negligible [33–35], whereas the computation cost for M3 was more than twice that of M2, and the computation cost for M4 was three times that of M2. Therefore, considering the calculation accuracy and time consumption comprehensively, the M2 grid was adopted in the subsequent numerical simulation.

Table 1. Verification of grid independence (L/D = 1.5, G/D = 3.0, ζ = 0, m^* = 10, and U_r = 6.0).

Mesh	Mesh Parameter			Downstream Cylinder–Plate Body				
	N_c	N_{pe}	N_{be}	A^*	f^*	$C_{D\text{-}ave}$	$C_{L\text{-}rms}$	Computation Cost (Hours per Cycle)
M1	172	6966	30,340	0.398	0.925	0.728	0.998	0.64
M2	220	11,130	47,061	0.399	0.925	0.733	0.974	0.86
M3	316	20,502	79,788	0.400	0.925	0.737	0.957	1.89
M4	563	46,666	14,9476	0.399	0.925	0.735	0.964	2.48

3.2. Numerical Method Verification

For the purpose of verifying the accuracy of the numerical method adopted in this paper, the flow around a single cylinder (Re = 200) was simulated numerically. Table 2 shows a comparison between the simulation results presented in this paper and the experimental and numerical simulation results presented in other literature sources. St, $C_{L\text{-}rms}$, and $C_{D\text{-}ave}$ are the Strouhal number, root-mean-square lift coefficient, and time-averaged drag coefficient, respectively. It can be seen from Table 2 that the calculated results in this paper are in good agreement with those outlined in other literature sources. However, due to the simplification of the calculation model in two-dimensional numerical simulation, there is a slight deviation between the numerical results and the experimental results. Overall, the method accurately simulates the FIV of a single bare cylinder.

Table 2. Accuracy verification of different numerical methods.

	Method	$C_{D\text{-}ave}$	$C_{L\text{-}rms}$	St
Present study	Numerical simulation	1.35	0.48	0.195
Wieselsberger [36]	Model test	1.29	—	—
Qu et al. [37]	Numerical simulation	1.32	0.46	0.196
Amini and Zahed [26]	Numerical simulation	1.31	0.46	0.196

In addition, the numerical simulation results of this study were compared with the results of cylinder–plate body flow-induced vibration found in the study by Sahu et al. [24]. The constraint form of the elastically mounted cylinder–plate body and the model parameters selected are consistent with reference [24]. The calculated results are shown in Figure 3. The results of dimensionless amplitude A^* and frequency ratio f^* calculated in this paper are essentially consistent with those of Sahu et al. [24], and the U_r of VIV response transforming into galloping response is also consistent. Zhao et al. [28] also proved the correctness of this conclusion. As shown in Figure 4, the present results were compared with the FIV of tandem cylinders with additional splitter plates in a study by Amini and Zahed [26], and the results were in good agreement. In reference [26], the upstream cylinder is a bare cylinder, and the downstream cylinder is attached with a splitter plate on the wake side. Both cylinders act as elastic installation, and the parameters are set as follows: Re = 150, ζ = 0, m^* = 2, G/D = 3, and L/D = 1. This demonstrates that the numerical method used in this paper has high accuracy and can accurately simulate the FIV of a cylinder.

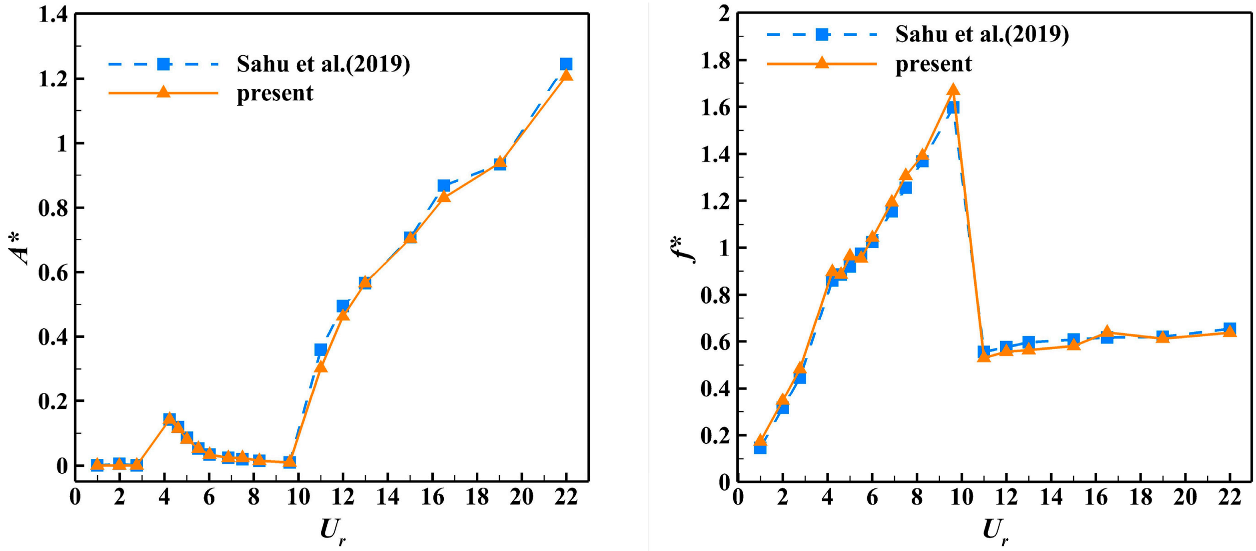

Figure 3. Verification results of A^* and f^* of a cylinder–plate body against the reduced velocity U_r [24].

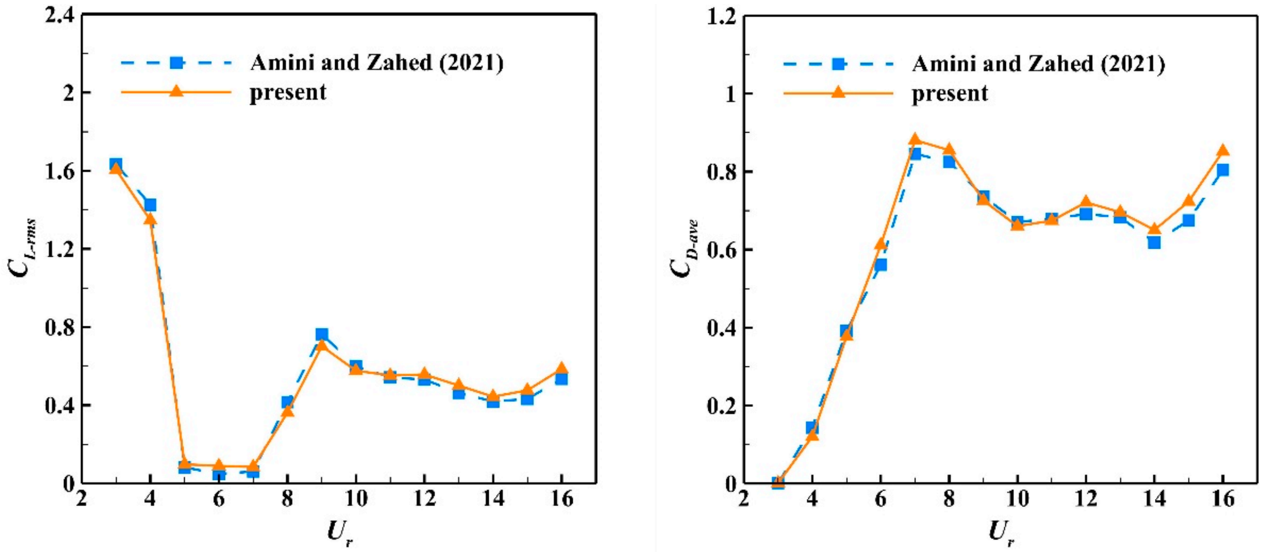

Figure 4. Verification results of the $C_{L\text{-}rms}$ and $C_{D\text{-}ave}$ of a cylinder–plate body against the reduced velocity U_r [26].

4. Results and Discussion

4.1. Response Amplitude and Frequency

The variation curves of A^* and f^* of the downstream cylinder (DC) and downstream additional splitter plate cylinder against U_r are shown in Figures 5a and 5b, respectively. The variations in the response regimes at different splitter plate additional positions against U_r are shown in Table 3.

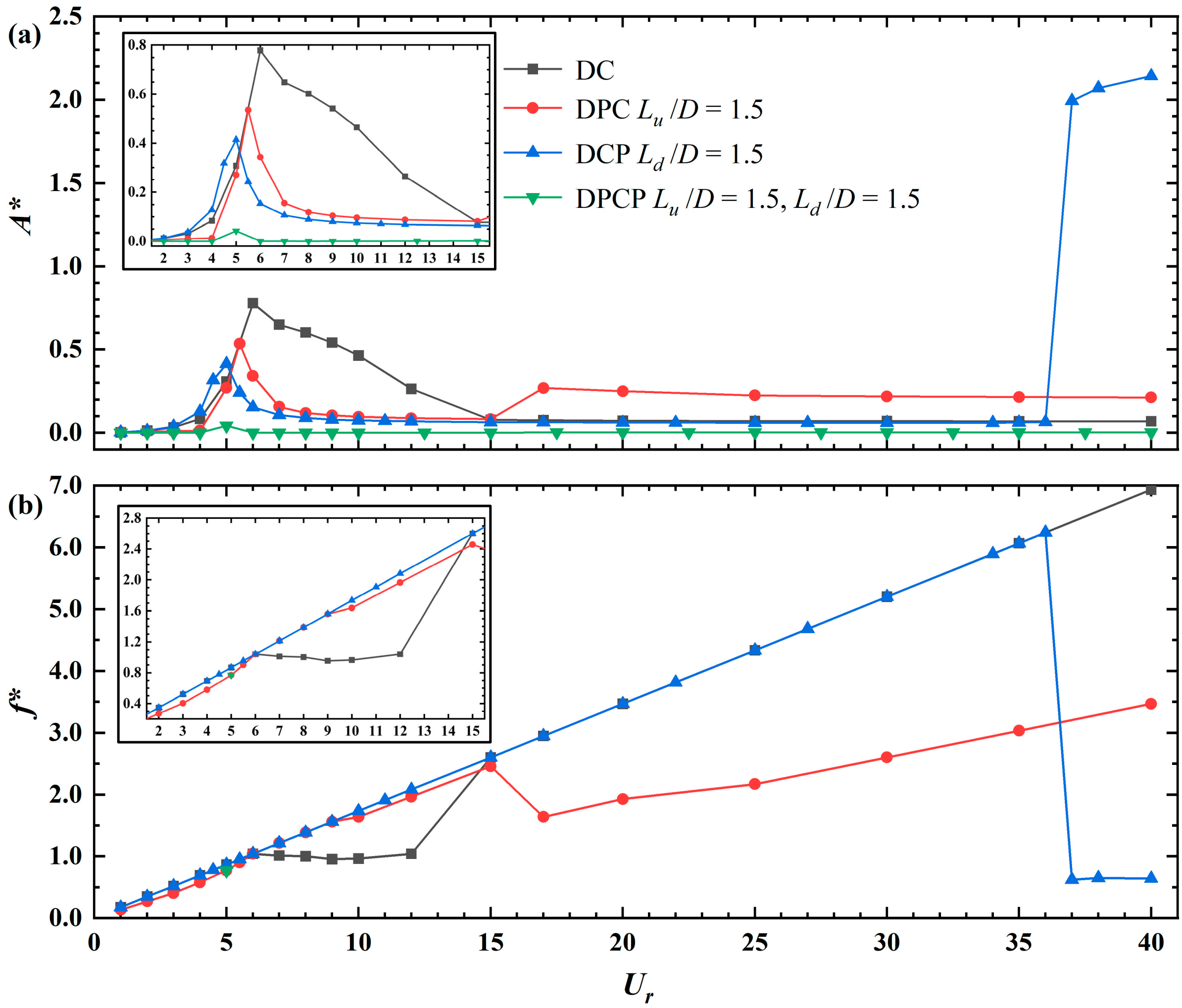

Figure 5. Variations of A^* and f^* at different splitter plate additional positions against U_r.

Table 3. Variations in the response regimes at different splitter plate additional positions against U_r.

	Stationary Flow	VIV	Galloping
DC	–	$1.0 \le U_r \le 40.0$	–
DPC	–	$1.0 \le U_r \le 40.0$	–
DCP	–	$1.0 \le U_r \le 36.0$	$U_r > 36.0$
DPCP	$1.0 \le U_r < 5.0$; $5.0 < U_r \le 36.0$	$U_r = 5.0$	–

For the DC, when $1.0 \le U_r < 5.0$, the vibration amplitude gradually grows with the growth of U_r. When $U_r = 5.0$, the DC response enters the lock-in region ($5.0 \le U_r < 15.0$); its amplitude firstly increases sharply with the increase in U_r and then gradually decreases after reaching the maximum amplitude $A^*_{\max} = 0.78$ ($U_r = 6.0$), while its vibration frequency is always locked near the natural frequency, that is, $f^* \approx 1.0$. When $U_r \ge 15.0$, the DC response enters the de-synchronization region, its amplitude remains almost constant as U_r enlarges, and the vibration frequency increases as U_r enlarges.

For the DPC, within the lock-in region ($4.0 < U_r \le 10.0$), its amplitude is proportional to U_r and gradually decreases after reaching the maximum amplitude $A^*_{max} = 0.54$ ($U_r = 5.5$). Compared with the DC, its maximum vibration amplitude decreases by 30.8%, and its lock-in bandwidth is also significantly narrower. And when $U_r > 17.0$, the vibration amplitude of the DPC increases slightly, while the vibration frequency decreases slightly.

For the DCP, the amplitude variation in the lock-in region ($4.0 < U_r \le 10.0$) is similar to that of the DPC, with the maximum amplitude $A^*_{\max} = 0.41$ ($U_r = 5$), and the maximum vibration amplitude decreases by 47.4% compared with the DC. Over the entire range of VIV response regimes, the vibration frequency of the DCP increases linearly with the increase in U_r. But when U_r is higher (U_r > 36.0), as shown in Table 3, the DCP will present a galloping response, and its vibration amplitude suddenly jumps to a higher level and grows continuously with the growth of U_r, while the frequency decreases to a lower level and remains almost constant with the increase in U_r.

For the DPCP, its maximum amplitude A^*_{max} = 0.05 (U_r = 5.0) decreased by 93.6% compared with the DC. When U_r = 5.0, the response mode of the DPCP is VIV with a small amplitude, and the vibration response is in an almost suppressed state under other reduced velocities. The vibration caused by the disturbance of wake flow is negligible.

4.2. Hydrodynamic Coefficients

The variation curves of the $C_{D\text{-}ave}$ and $C_{L\text{-}rms}$ of the downstream cylinder–plate body at different splitter plate additional positions against U_r are shown in Figures 6a and 6b, respectively. For the DC, with U_r increasing from 1.0 to 5.0, its $C_{L\text{-}rms}$ gradually increases to the maximum value of 1.5. After reaching the maximum value, its $C_{L\text{-}rms}$ slightly decreases and then it remains almost unchanged with U_r increasing. Its $C_{D\text{-}ave}$ increases slightly with the increase in U_r and increases substantially near the starting point of lock-in, reaching a maximum value of 1.1 when U_r = 6, and rapidly decreases after reaching the maximum value until the ending point of lock-in. When $U_r \geq 15.0$, its $C_{D\text{-}ave}$ remains almost constant with the increase in U_r.

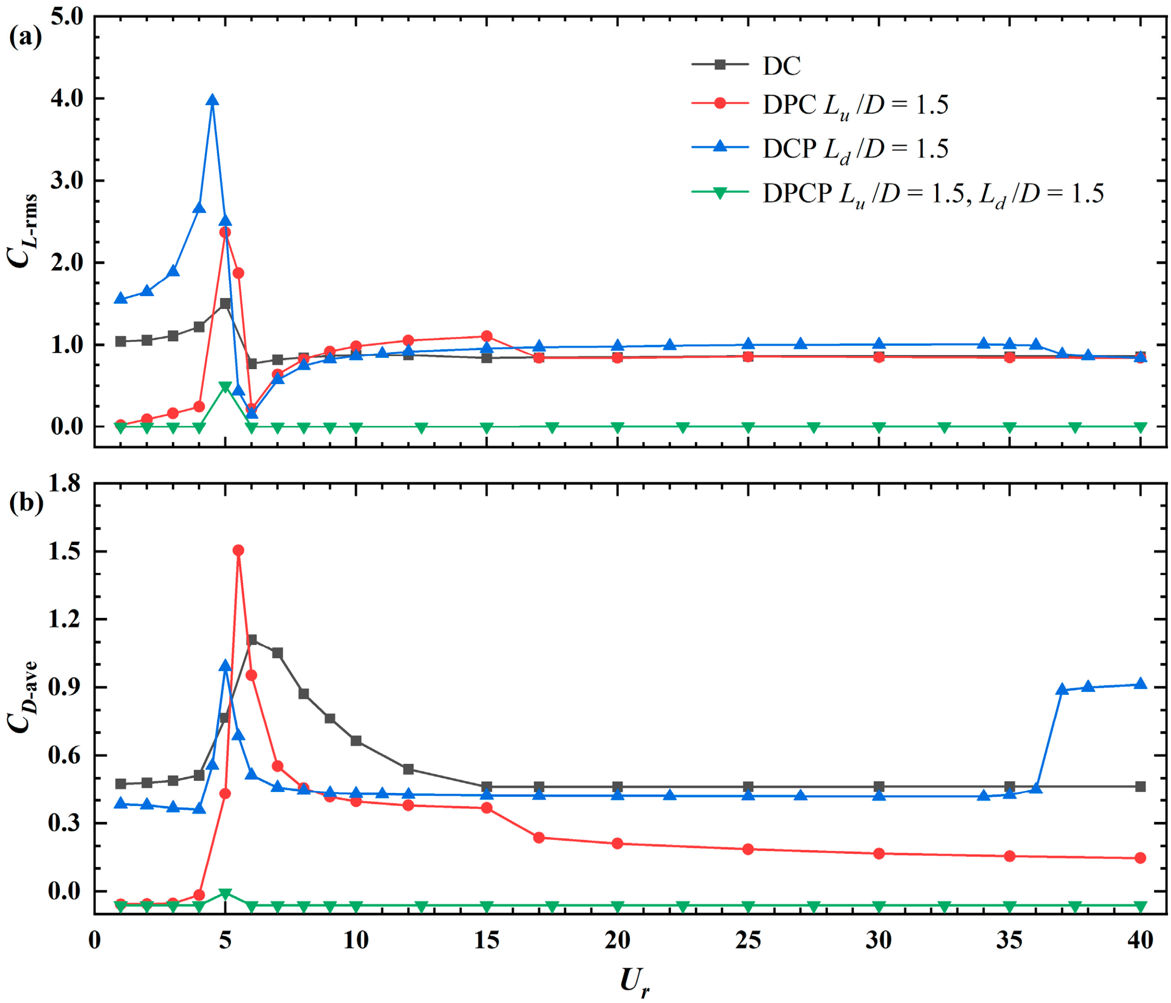

Figure 6. Variations in the $C_{L\text{-}rms}$ and $C_{D\text{-}ave}$ at different splitter plate additional positions against U_r.

For the DPC and the DCP, the variation trend of $C_{L\text{-}rms}$ is similar to that of the DC, but the maximum $C_{L\text{-}rms}$ is significantly larger than that of the DC because of the splitter plate. The maximum value of the $C_{L\text{-}rms}$ of the DPC is 2.3, and the maximum value of $C_{L\text{-}rms}$ is increased by 53.3% compared with the DC. The maximum value of the $C_{L\text{-}rms}$ of the DCP is 4.0, and the maximum value of $C_{L\text{-}rms}$ is increased by 166.6% compared with the DC. The $C_{D\text{-}ave}$ of the DPC greatly increases with the increase in U_r, reaching a maximum value of 1.5 when $U_r = 6$, and rapidly decreases after reaching the maximum value until the end of lock-in. When $U_r \geq 15.0$, its $C_{D\text{-}ave}$ decreases with the increase in U_r. Compared with the DC, the maximum $C_{D\text{-}ave}$ increases by 36.4%. The change trend of $C_{D\text{-}ave}$ in the lock-in region of the DCP is similar to that of the DPC, reaching a maximum value of 1.0 when $U_r = 5$. Compared with the DC, the maximum average drag coefficient decreases by 9.1%. When $15.0 \leq U_r < 36.0$, its $C_{D\text{-}ave}$ almost remains unchanged with the increase in U_r. When $U_r \geq 36.0$, its $C_{D\text{-}ave}$ increases rapidly due to the generation of galloping response. For the DPCP, except $U_r = 5.0$, the $C_{L\text{-}rms}$ of the DPCP remains around zero at other reduced velocities, and the $C_{D\text{-}ave}$ is slightly less than zero.

4.3. Wake Patterns

To clarify the fluid–structure interaction mechanism of the cylinder–plate body with different additional modes under wake interference, the typical instantaneous vorticity contours of structures with different response branches at the maximum displacement time were selected, as shown in Figures 7 and 8.

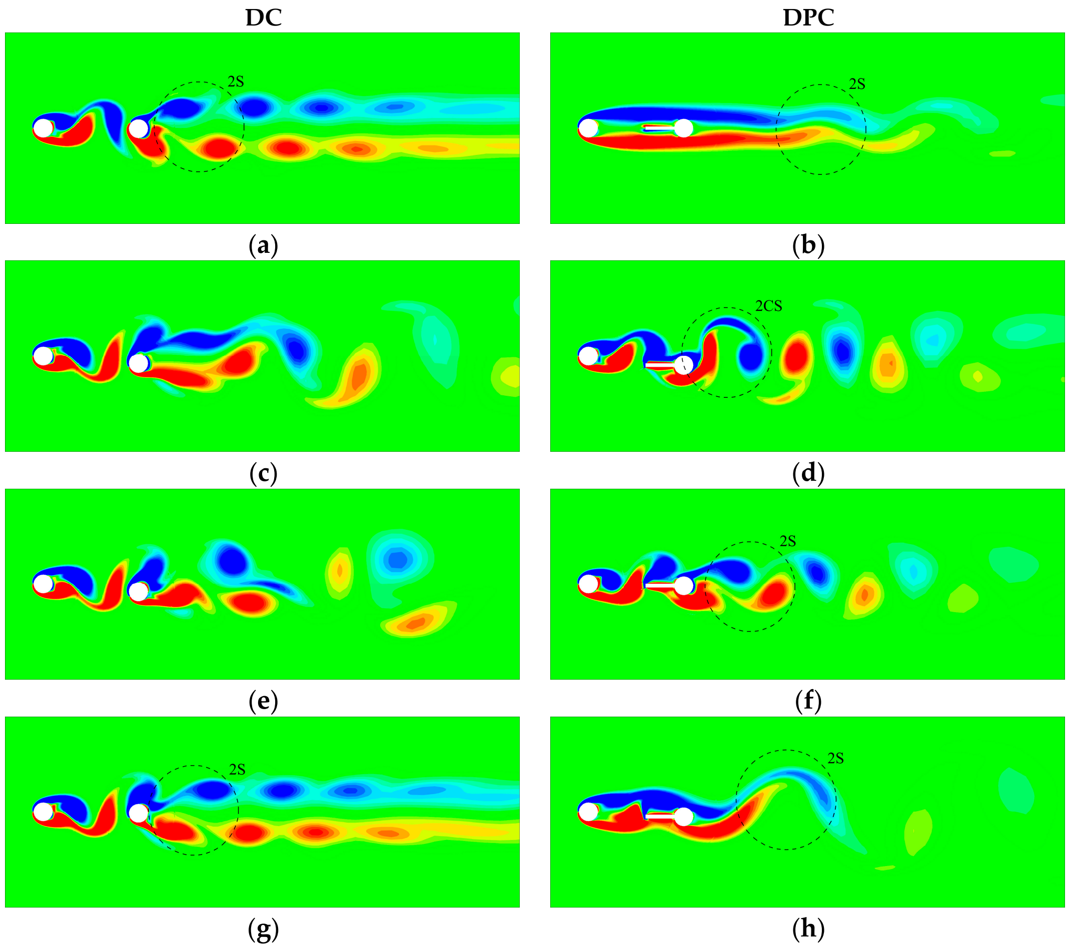

Figure 7. *Cont.*

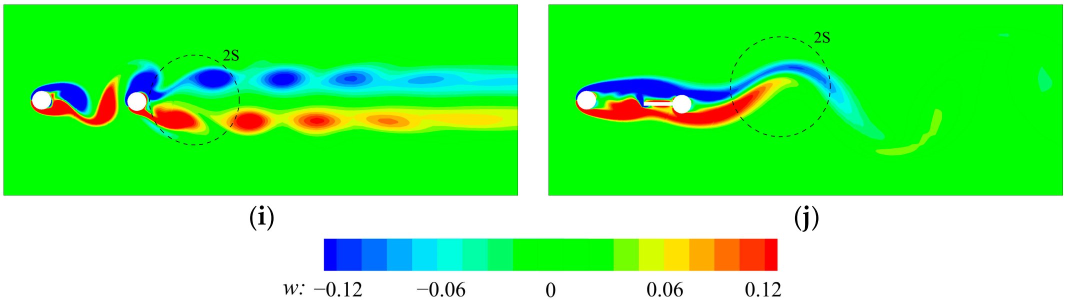

Figure 7. Instantaneous vorticity contours at various U_r (DC and DPC). (**a**) U_r = 3.0; (**b**) U_r = 3.0; (**c**) U_r = 6.0; (**d**) U_r = 5.5; (**e**) U_r = 10.0; (**f**) U_r = 10.0; (**g**) U_r = 15.0; (**h**) U_r = 17.0; (**i**) U_r = 40.0; (**j**) U_r = 40.0.

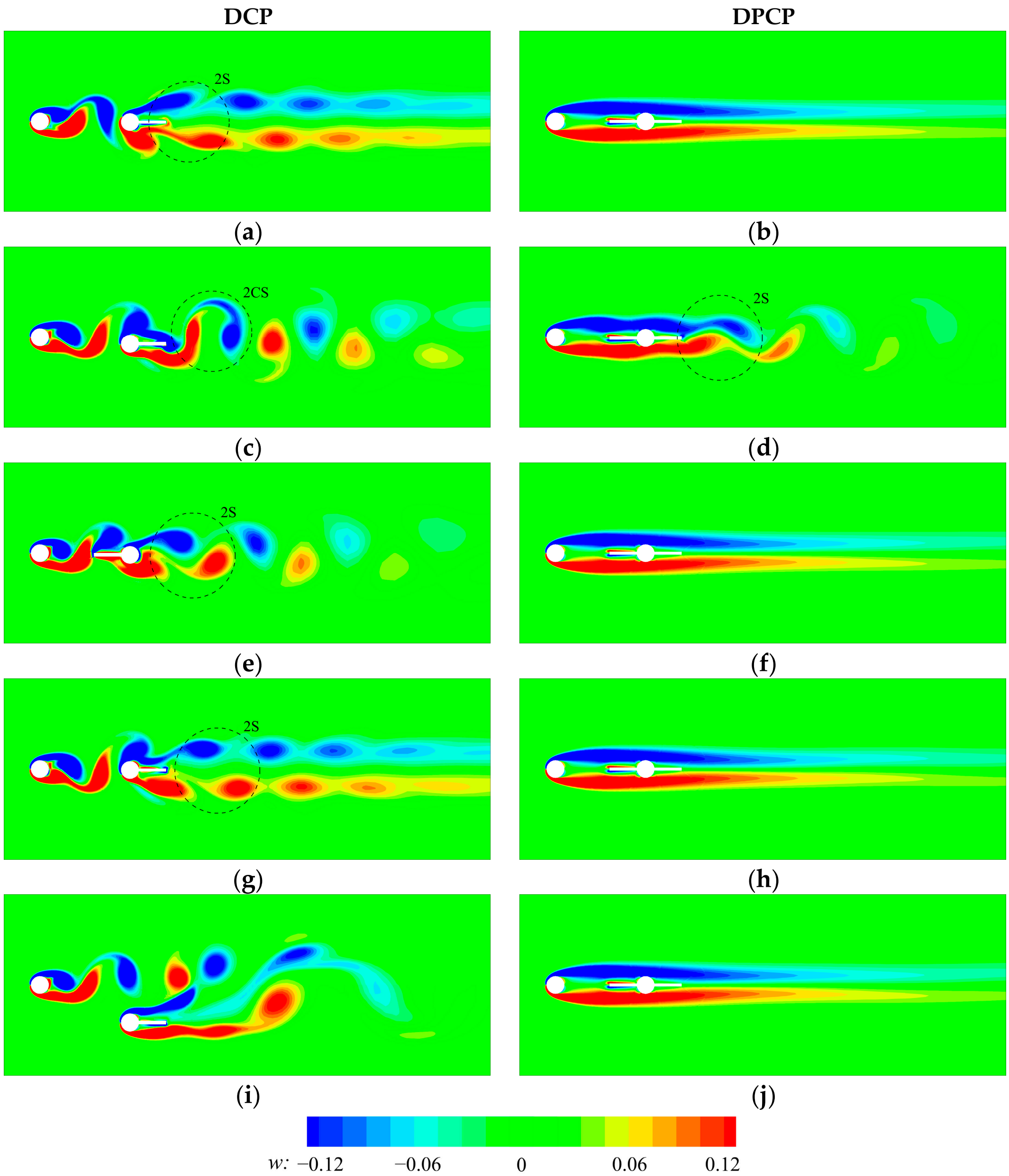

Figure 8. Instantaneous vorticity contours at various U_r (DCP and DPCP). (**a**) U_r = 3.0; (**b**) U_r = 3.0; (**c**) U_r = 5.0; (**d**) U_r = 5.0; (**e**) U_r = 10.0; (**f**) U_r = 10.0; (**g**) U_r = 15.0; (**h**) U_r = 15.0; (**i**) U_r = 40.0; (**j**) U_r = 40.0.

For the DC, as shown in Figure 7a, when U_r is low ($1.0 \leq U_r < 5.0$), the wake vortex street of the downstream cylinder is symmetrical, and the shedding mode of the wake vortex is 2S. As depicted in Figure 7c,e, with the response of the DC entering the lock-in region ($5.0 \leq U_r < 15.0$), its vortex shedding is not synchronized with the upstream cylinder, and the shedding vortex from the upstream cylinder impinges on the DC, which causes the DC to generate a large amplitude within the lock-in region. As shown in Figure 7g,i, when $U_r \geq 15.0$, the response of the DC enters the de-synchronization zone, and the vortex shedding mode is in the symmetrical 2S mode. Shedding of a pair of vortices in opposite rotation directions within a period is characteristic of this mode, and the vortex strength is weak, so its amplitude in the de-synchronization range is very small.

For the DPC, as shown in Figure 7b, when U_r is low ($1.0 \leq U_r \leq 4.0$), the free shear layer around the upstream cylinder completely wraps the DPC, the separated shear layer behind the DPC is elongated, and the position of the vortex shedding is further away. In this wake mode, the DPC is subjected to little resistance and lift. The amplitude of the vibration generated by the wake flow disturbance is negligible. As shown in Figure 7d, with the DPC response entering the lock-in region ($4.0 < U_r \leq 10.0$), the contribution of upstream vortex shedding causes a vortex shedding mode of 2CS to appear behind the DPC, but as shown in Figure 7f, with the further enlargement of U_r, the wake mode quickly switches back to the 2S mode until the lock-in ends. As shown in Figure 7h,j, when $U_r \geq 17.0$, the DPC is completely wrapped by the free shear layer of the upstream cylinder and no longer rolls up. Different from the wake mode at low U_r, the upstream shear layer is not symmetrical, but swings up and down with the vibration of the DPC, and the gap flow between the cylinders switches back and forth on both sides of the DPC. This switching of the gap flow helps to maintain its vibration, and as a result, the response amplitude of the DPC is observed to increase slightly outside the lock-in bandwidth.

For the DCP, as shown in Figure 8a, when U_r is low ($1.0 \leq U_r < 4.0$), the vortices are formed by rolling up the separated shear layer of the upstream cylinder, and the vortex “strikes” the DCP and merges with the vortex generated by the DCP. After the vortices merge, the wake vortex street shows a 2S mode. As shown in Figure 8c, when U_r increases to 5.0, the wake vortex street of the structure shows a 2CS mode because of the influence of the upstream cylinder wake vortices. As shown in Figure 8g, with the further enlargement of U_r, the vortex shedding mode quickly switches back to 2S mode, which remains unchanged with the increase in U_r until the end of the de-synchronization phase. As shown in Figure 8i, when $U_r > 36.0$, the response mode of the DCP changes from VIV to galloping, the relative position of the upstream cylinder and the DCP in the cross-flow direction changes greatly, and the separation shear layer of the DCP tilts in the forward-flow direction and reattaches to the wake-side splitter plate. In addition, the vortices shed from the DCP are obviously elongated and merged with the vortices shed from the upstream cylinder to form a new wake vortex street.

For the DPCP, when U_r is low ($1.0 \leq U_r < 5.0$), the double splitter plate structure can transfer the layer shear separation point of the upstream cylinder to the downstream cylinder, so that the separated shear layer of the DPCP is completely parallel to the free flow, accompanied by no vortex shedding. When $U_r = 5.0$, the upstream shear layer is still completely parallel to the free flow. Although the DPCP structure can form shedding vortices, the vortex strength is extremely weak, and the vibration amplitude caused by it is very small. When $U_r > 5.0$, the wake pattern is almost the same as that at low U_r, the shear layer is completely parallel to the free stream without separation, and the vibration generated by the DPCP under flow disturbance is negligible.

5. Conclusions

In this study, numerical simulation was used to study the fluid–structure interaction problem of an elastically mounted cylinder–plate body under the impact of the wake of a fixed upstream cylinder. The effects of the rigid splitter plate at distinct additional positions on the FIV of the downstream cylinder were analyzed and discussed at a fixed spacing ratio (G/D = 5.0) and a low Reynolds number (Re = 150). The main conclusions are listed as follows:

The addition of the splitter plate on the incoming flow or wake side can suppress the vibration of the downstream cylinder within a certain reduced velocity range. Compared with the DC, the maximum response amplitude of the DPC and the DCP in the lock-in region ($4.0 < U_r \leq 10.0$) is reduced by 30.8% and 47.4%, respectively, and the lock-in bandwidth is significantly narrower. When the reduced velocities are outside the lock-in region, gap flow switching between cylinders results in a larger response amplitude for the DPC than for downstream cylinders. At high reduced velocity ($U_r > 36.0$), the DCP will show a galloping response, maintain a high response amplitude, and increase with an increase in U_r.

The suppression effect of FIV is optimal when splitter plates are attached to both the incoming flow and wake sides of the downstream cylinder. The maximum response amplitude of the DPCP is reduced by 93.6% compared with that of the DC. The double splitter plate structure can transfer the layer shear separation point of the upstream cylinder to the downstream cylinder, so that the separated shear layer of the DPCP is completely parallel to the free flow. When U_r = 5.0, the response mode of the DPCP is VIV with a small amplitude, and the vibration response is in an almost suppressed state under other reduced velocities.

Author Contributions: Data curation, formal analysis, methodology, validation, writing: original draft: L.R.; funding acquisition, supervision: D.Y.; formal analysis, methodology, validation: J.B.; conceptualization, software, data curation: J.Z. All authors have read and agreed to the published version of the manuscript.

Funding: This research was funded by National Natural Science Foundation of China (51739010).

Institutional Review Board Statement: Not applicable.

Informed Consent Statement: Not applicable.

Data Availability Statement: Data are contained within the article.

Conflicts of Interest: The authors declare no conflict of interest.

References

1. Zheng, H.; Price, R.E.; Modarres-Sadeghi, Y.; Triantafyllou, M.S. On fatigue damage of long flexible cylinders due to the higher harmonic force components and chaotic vortex-induced vibrations. *Ocean Eng.* **2014**, *88*, 318–329. [CrossRef]
2. Liu, G.; Li, H.; Qiu, Z.; Leng, D.; Li, Z.; Li, W. A mini review of recent progress on vortex-induced vibrations of marine risers. *Ocean Eng.* **2020**, *195*, 106704.
3. Bernitsas, M.M.; Ben-Simon, Y.; Raghavan, K.; Garcia EM, H. The VIVACE Converter: Model Tests at High Damping and Reynolds Number Around 105. *J. Offshore Mech. Arct. Eng.* **2009**, *131*, 011102. [CrossRef]
4. Choi, H.; Jeon, W.P.; Kim, J.S. Control of Flow Over a Bluff Body. *Annu. Rev. Fluid Mech.* **2008**, *40*, 113–139. [CrossRef]
5. Muddada, S.; Paynaik BS, V. Active flow control of vortex induced vibrations of a circular cylinder subjected to non-harmonic forcing. *Ocean Eng.* **2017**, *142*, 62–77. [CrossRef]
6. Dehkordi, B.G.; Jafari, H.H. On the Suppression of Vortex Shedding From Circular Cylinders Using Detached Short Splitter-Plates. *J. Fluids Eng. Trans. ASME* **2010**, *132*, 044501. [CrossRef]
7. Holland, V.; Tezdogan, T.; Oguz, E. Full-scale CFD investigations of helical strakes as a means of reducing the vortex induced forces on a semi-submersible. *Ocean Eng.* **2017**, *137*, 338–351. [CrossRef]
8. Zheng, H.; Wang, J. Numerical study of galloping oscillation of a two-dimensional circular cylinder attached with fixed fairing device. *Ocean Eng.* **2017**, *130*, 274–283. [CrossRef]
9. Fang, S.M.; Niedzwecki, J.M.; Fu, S.; Li, R.; Yang, J. VIV response of a flexible cylinder with varied coverage by buoyancy elements and helical strakes. *Mar. Struct.* **2014**, *39*, 70–89. [CrossRef]
10. Wang, J.; Zheng, H.; Tian, Z. Numerical simulation with a TVD-FVM method for circular cylinder wake control by a fairing. *J. Fluid Struct.* **2015**, *57*, 15–31. [CrossRef]
11. Roshko, A. On the wake and drag of bluff bodies. *J. Aeronaut. Sci.* **1955**, *22*, 124–132. [CrossRef]
12. Apelt, C.J.; West, G.S. The effects of wake splitter plates on bluff-body flow in the range $10^4 < \mathrm{Re} < 5 \times 10^4$. Part 2. *J. Fluid Mech.* **1975**, *71*, 145–160.
13. Kwon, K.; Choi, H. Control of laminar vortex shedding behind a circular cylinder using splitter plates. *Phys. Fluids* **1996**, *8*, 479–486. [CrossRef]

14. Hu, Z.; Wang, J.; Sun, Y.; Zheng, H. Flow-induced vibration suppression for a single cylinder and one-fixed-one-free tandem cylinders with double tail splitter plates. *J. Fluids Struct.* **2021**, *106*, 103373. [CrossRef]
15. Sun, X.; Suh, C.S.; Ye, Z.H.; Yu, B. Dynamics of a circular cylinder with an attached splitter plate in laminar flow: A transition from vortex-induced vibration to galloping. *Phys. Fluids* **2020**, *32*, 027104. [CrossRef]
16. Zhu, H.J.; Liu, W.L. Flow control and vibration response of a circular cylinder attached with a wavy plate. *Ocean Eng.* **2020**, *212*, 107537. [CrossRef]
17. Nemes, A.; Zhao, J.; Jacono, D.L.; Sheridan, J. The interaction between flow-induced vibration mechanisms of a square cylinder with varying angles of attack. *J. Fluid Mech.* **2012**, *710*, 102–130. [CrossRef]
18. Zhao, J.; Leontini, J.S.; Jacono, D.L.; Sheridan, J. Fluid-structure interaction of a square cylinder at different angles of attack. *J. Fluid Mech.* **2014**, *747*, 688–721. [CrossRef]
19. Zhao, J.; Leontini, J.; Jacono, D.L.; Sheridan, J. The effect of mass ratio on the structural response of a freely vibrating square cylinder oriented at different angles of attack. *J. Fluids Struct.* **2019**, *86*, 200–212. [CrossRef]
20. Zhao, J.; Hourigan, K.; Thompson, M.C. An experimental investigation of flow-induced vibration of high-side-ratio rectangular cylinders. *J. Fluids Struct.* **2019**, *91*, 102580. [CrossRef]
21. Zhu, H.J.; Li, G.M.; Wang, J.L. Flow-induced vibration of a circular cylinder with splitter plates placed upstream and downstream individually and simultaneously. *Appl. Ocean Res.* **2020**, *97*, 102084. [CrossRef]
22. Cui, G.P.; Feng, L.H.; Hu, Y.W. Flow-induced vibration control of a circular cylinder by using flexible and rigid splitter plates. *Ocean Eng.* **2022**, *249*, 110939. [CrossRef]
23. Diaz-Ojeda HRGonzalez LMHuera-Huarte, F.J. On the influence of the free surface on a stationary circular cylinder with a flexible splitter plate in laminar regime. *J. Fluids Struct.* **2019**, *87*, 102–123.
24. Sahu, T.R.; Furquan, M.; Jaiswal, Y.; Mittal, S. Flow-induced vibration of a circular cylinder with rigid splitter plate. *J. Fluids Struct.* **2019**, *89*, 244–256. [CrossRef]
25. Sun, Y.; Wang, J.; Fan, D.; Zheng, H.; Hu, Z. The roles of rigid splitter plates in flow-induced vibration of a circular cylinder. *Phys. Fluids* **2022**, *34*, 114114. [CrossRef]
26. Amini, Y.; Zahed, I. Flow-induced vibration of two tandemly arranged circular cylinders with attached splitter plates. *Ocean Eng.* **2021**, *237*, 109604. [CrossRef]
27. Assi GR, S.; Bearman, P.W.; Kitney, N. Low drag solutions for suppressing vortex-induced vibration of circular cylinders. *J. Fluids Struct.* **2009**, *25*, 666–675. [CrossRef]
28. Zhao, J.X.; Yu, D.Y.; Bao, J.; Gong, M.J. The effect of spacing on the flow-induced vibration of one-fixed-one-free tandem cylinders with a rigid splitter plate. *Ocean Eng.* **2023**, *281*, 114722. [CrossRef]
29. Placzek, A.; Sigrist, J.; Hamdouni, A. Numerical simulation of an oscillating cylinder in a cross-flow at low Reynolds number: Forced and free oscillations. *Comput. Fluids* **2009**, *38*, 80–100. [CrossRef]
30. Xu, W.H.; Wu, H.K.; Jia, K.; Wang, E.H. Numerical investigation into the effect of spacing on the flow-induced vibrations of two tandem circular cylinders at subcritical Reynolds numbers. *Ocean Eng.* **2021**, *236*, 109521. [CrossRef]
31. Merrill, B.E.; Peet, Y.T. Moving overlapping grid methodology of spectral accuracy for incompressible flow solutions around rigid bodies in motion. *J. Comput. Physics.* **2019**, *390*, 121–151. [CrossRef]
32. Huang, J.B.; Bathe, K.J. Overlapping Finite Elem. Meshes AMORE. *Adv. Eng. Softw.* **2020**, *144*, 102791. [CrossRef]
33. Chen, D.Y.; Marzocca, P.; Xiao, Q.; Zhan, Z.H.; Gu, C.J. Vortex-induced vibration on a low mass ratio cylinder with a nonlinear dissipative oscillator at moderate Reynolds number. *J. Fluids Struct.* **2020**, *99*, 103160. [CrossRef]
34. Wang, E.H.; Zhao, S.H.; Xu, W.H.; Xiao, Q.; Li, B. Effect of splitter plate length on FIV of circular cylinder. *Int. J. Mech. Sci.* **2023**, *254*, 108413. [CrossRef]
35. Zhu, H.J.; Chen, Q.Y.; Tang, T.; Alam, M.M.; Zhou, T.M. Flow structures around a circular cylinder with bilateral splitter plates and their dynamic characteristics. *Ocean Eng.* **2023**, *269*, 113547. [CrossRef]
36. Von Wieselsberger, C. Neuere Festellungen über die Gesetze des Flüssigkeits un Luftwiderstands. *Phys. Z.* **1921**, *22*, 321–328.
37. Qu, L.; Norberg, C.; Davidson, L.; Peng, S.-H.; Wang, F. Quantitative numerical analysis of flow past a circular cylinder at Reynolds number between 50 and 200. *J. Fluids Struct.* **2013**, *39*, 347–370. [CrossRef]